Alternative Tilings for Improved Surface Area Estimates by Local Counting Algorithms

Erik G. Miller

Massachusetts Institute of Technology
Artificial Intelligence Laboratory

Running Head: Improved Surface Area Estimates

Correspondence information:
Erik G. Miller
545 Technology Square, Office 769
Cambridge MA 02139

Phone: (617) 253-6723
Fax: (617) 253-5060

Abstract

In this paper, we first review local counting methods for perimeter estimation of piecewise smooth binary figures on square, hexagonal, and triangular grids. We verify that better perimeter estimates, using local counting algorithms, can be obtained using hexagonal or triangular grids. We then compare surface area estimates using local counting techniques for binary three-dimensional volumes under the three semi-regular polyhedral tilings: the cubic, truncated octahedral, and rhombic dodecahedral tilings. It is shown that for surfaces of random orientation with a uniform distribution, the expected error of surface area estimates is smaller for the truncated octahedral and rhombic dodecahedral tilings than for the standard cubic or rectangular prism tilings of space. Additional properties of these tessellations are reviewed and potential applications of better surface area estimates are discussed.

Math Symbols

Less than	$<$
Prime marking	$'$
Square Root	$\sqrt{2}$
Approximately Equal	$\approx$
Integral Sign	$\int$
For All	$\forall$
Equals	$=$
Membership	$\in$
Division	$/$
Summation	$\sum$

Greek Letters

Lowercase Pi	π
Lowercase Phi	ϕ
Lowercase Theta	θ
Lowercase Epsilon	ε

1. Introduction

To represent images or volumes in a digital computer, they must be discretized. This discretization leads to errors in the computation of such fundamental properties of objects as perimeter, area, volume, and surface area. Not surprisingly, the magnitudes of these errors depend upon the particular discretization used. There are an infinite variety of discrete approximations for any planar figure, from the spatial frequency decompositions used in signal processing to parameterized NURB surfaces used in the CAD/CAM world. In this paper, we focus on a particular class of discretizations: the *tessellation* of planar figures and solid volumes. Tessellations are approximate representations particularly convenient in computer vision and graphics.

1.1. Some Definitions

We define the *tessellation of a figure* (in either two or three dimensions) as the discretization of the figure into a finite number of continuous regions, each having a constant value (See Figure 1). The value of each region is some measure of the original figure in that vicinity, such as a point sample of the figure at the centroid of the region or a spatial average over the region. In two dimensions, these regions are typically dubbed *pixels*, for picture elements, and in three dimensions *voxels*, for volume elements. In this paper, a pixel in a tessellated figure will be labelled black if some non-zero measure portion of its interior is black in the original image. Otherwise, it will be labelled white.

We use the term *tiling* synonymously with tessellation, and each element of a tessellation is sometimes referred to as a *tile*, especially if the dimension is unspecified. The term *grid* shall be used to denote the specific arrangement of tiles used to cover a space. For example, squares can be placed in the common Cartesian grid (like ordinary graph paper), or can be arranged so that each row is offset by some distance from the previous row (as in a brick wall). When discussing a square grid, a Cartesian grid will be assumed unless otherwise stated.

In the following analyses, we restrict our focus to *binary* images and volumes, i.e. data sets in which each pixel or voxel has one of two values (black or white, 0 or 1, etc.). Much

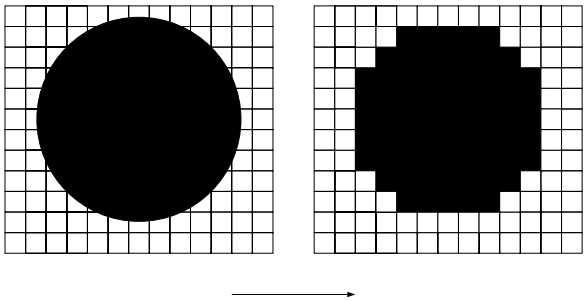

Figure 1: The tessellation of a circle on a square grid. Here, the original figure was sampled at the center of each tile, and this value was copied across the whole tile. The figure on the left is a *continuous binary image*. The figure on the right is a *discrete binary image*.

of the previous work on properties of tessellations does the same: [2, 5, 6, 8]. Prior to tessellation we call a binary image *continuous*. After tessellation, it becomes a *discrete* binary image. The same terminology applies to volumes.

1.2. Local Counting Algorithms

Much of the work in discrete binary image processing has focused on *local counting algorithms* [6, 9]. These techniques involve computing functions of figures when only local image information is available for computations, and local results are reported to a global accumulator. For example, in a black and white image, the perimeter of a tessellated figure can be computed using a local counting scheme as follows: a processor at each black pixel reports to the global accumulator the length of its border with neighboring white pixels. The sum of the results from each processor is the exact perimeter of the tessellated figure. It is also a *perimeter estimate* (not always a good one) of the originally imaged object from which the tessellated figure was derived. Local counting algorithms have been motivated in part by their inherent parallelism and simplicity of implementation, making them suitable for use on fine grain, highly parallel computers.

1.3. LCAP and ALCAP

While there are many local counting algorithms for computing perimeter, we restrict our attention here to the method described above, which we shall refer to as Local Counting Algorithm for Perimeter computation, or LCAP. The analyses which follow could be applied

to other local counting algorithms in a similar manner. To focus on the issue of pixel shape rather than size, we introduce the notion of the Asymptotic LCAP estimate of perimeter (ALCAP), which we define to be the limit of the LCAP estimate as the diameter of the grid pixels approaches zero. This is a simple way to enforce the condition that the grid pixels are "small enough" so that a particular grid shape is providing the best estimate it can.

One might assume that LCAP would produce zero-error perimeter estimates as the pixel size of the grid approaches zero. However, as is easily seen in Figure 2, it is not always true that increasing the resolution of the pixel grid improves our perimeter estimate. It is this fact which motivates us to try alternative grid pixel shapes in an effort to improve our LCAP perimeter estimates.

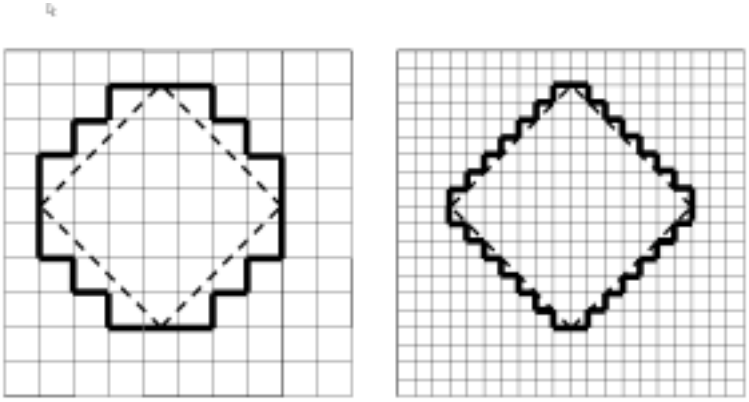

Figure 2: Coarse and fine tessellations of a figure. On the left, the dotted square has been tessellated at low resolution. On the right, the same square has been tessellated at a higher resolution. The LCAP perimeter estimates of the squares on the grids are numerically equal.

1.4. Pixel and Voxel Shapes

In Sections 2 and 3, we explore the performance of ALCAP using various shapes for the pixels and voxels in the tessellating grids. In two dimensions, we explore grids composed of the regular polygons which can tile the plane: the square, the regular hexagon, and the equilateral triangle. In three dimensions we explore grids composed of regular and semi-regular polyhedra and their duals. But how should we compare the performance of the different grids?

For a particular edge of a plane figure, LCAP produces results of differing accuracy depending upon the orientation of that edge. Hence, the performance of LCAP on a whole figure is dependent upon the distribution of orientations of edges in all of the sides of the figure. For example, on a square grid, the ALCAP estimate for an axis-aligned rectangle is perfect, for a rectangle at 45 degrees it is off by a factor of $\sqrt{2}$, and for a circle it is somewhere in between with an error factor of $4/\pi$. To get an expectation of the relative ALCAP error, one could specify a distribution over shapes $\mathcal{S}$ from which samples were drawn and then compute the expected error factor as

$$E_{\mathcal{S}}(error) = \sum_{S \in \mathcal{S}} p(S) * \frac{ALCAP(S)}{L(S)} \tag{1}$$

where $p(S)$ is the probability of drawing a particular sample S from $\mathcal{S}$ and $L(S)$ is the true Euclidean perimeter of S.

The problem with this approach is that it is difficult in most cases to come up with a reasonable approximation to $\mathcal{S}$, since it is rare that one can fully characterize the distribution of shapes in which one is interested. As an alternative we decided to examine the behavior of ALCAP in estimating lengths of straight border segments, since this gives a good measure of how sensitive each tiling is to the orientations of the sides of figures.

1.5. Random Line Segment Processes

In order to compare the performance of ALCAP using different tile shapes, we introduce a random process $\mathcal{P}$ whose samples are line segments of unit length and which form random angles θ (with uniform distribution) with the x-axis. We shall examine the expectation of various functions of ALCAP taken over $\mathcal{P}$. (Technically, ALCAP produces the *perimeter* of a line segment and not its length. When we refer to the "length" of a line segment, we are using this as a shorthand for the "length of a border defined by the line segment," which can be computed by ALCAP.)

1.6. Caveats

Before proceeding with our analyses of various grid pixel shapes on infinitely fine grids, we examine limitations of our analysis. Since we will be analysing the behavior of LCAP on an infinitely fine grid, we would incur additional errors in practice when using a finite grid. Below, we examine the types of additonal errors which can arise on a finite grid.

1.6.1. City Block Distance

On an infinitely fine square grid, ALCAP assigns to a straight edge e a length equal to the *city block distance* between the two vertices v^1 and v^2 defining the edge:

$$L_s(v^1, v^2) = |v_x^1 - v_x^2| + |v_y^1 - v_y^2|. \tag{2}$$

To compute the perimeter of an entire figure F we then have

$$L_s(F) = \sum_{i=0}^{N} L_s(v^i, v^{i+1}). \tag{3}$$

where v^0 and v^N name the same vertex for notational convenience. Now consider the set of all local extrema of the figure F relative to the x and y directions starting at v^0. These appear as the horizontal and vertical hashmarks in the left side of Figure 3. Let x^i be the x-coordinate of the ith extremum in the x direction. Let the total number of these extrema be X. Also, let y^i be the y-coordinate of the ith extremum in the y direction. Let the total number of these extrema be Y. We will call these x^i and y^i local *coordinate extrema*. Then we have

$$\begin{aligned} L_s(F) &= \sum_{i=0}^{N} L_s(v^i, v^{i+1}) && (4)\\ &= \sum_{i=0}^{N} |v_x^i - v_x^{i+1}| + |v_y^i - v_y^{i+1}| && (5)\\ &= \sum_{i=0}^{N} |v_x^i - v_x^{i+1}| + \sum_{i=0}^{N} |v_y^i - v_y^{i+1}| && (6) \end{aligned}$$

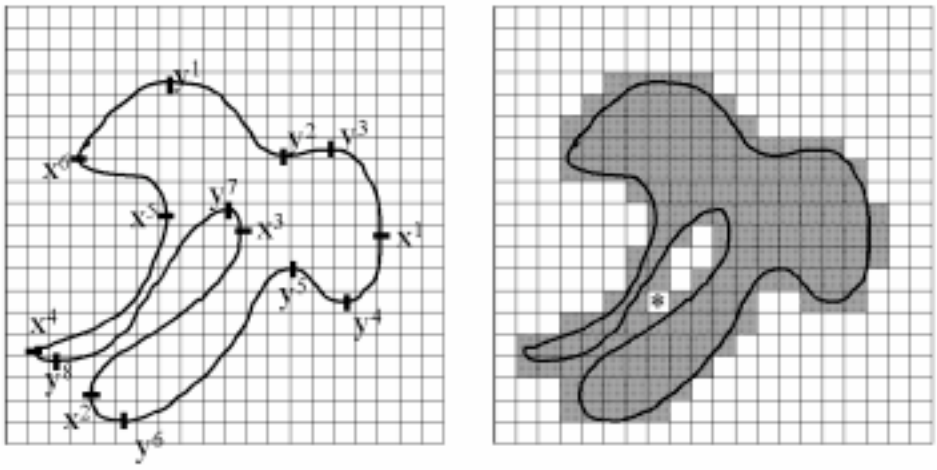

Figure 3: Effects of tessellation on the coordinate extrema of a figure. Some extrema (e.g. y^6) remain in the same position in the tessellated figure. Others (e.g. y^1) are shifted. Some disappear (y^2 and y^3). Topogical changes can cause new extrema to appear (*).

$$= \sum_{i=0}^{X} |x^i - x^{i+1}| + \sum_{i=0}^{Y} |y^i - y^{i+1}|. \tag{7}$$

Notice that in the last step, we replace a sum over all vertices with sums over the local coordinate extrema. This is possible since the signs of the quantities in the absolute value brackets will only change at extrema, eliminating all but the coordinate extrema terms in the sum. This applies even for figures with curved boundaries (and hence an infinite number of vertices).

An immediate consequence of the above result is that if a finite square grid G tessellates a continuous figure F into a discrete figure F' such that the local coordinate extrema of F' are equivalent to those of F, then the LCAP perimeter estimate of F' will be equivalent to the ALCAP perimeter estimate of F. Of course, for a finite grid, the above condition (equivalence of extrema) will not hold in general. When tessellating a figure F into F', this condition can break down in two ways: 1) either the coordinate extrema between the two figures can remain in one-to-one correspondence but be shifted from their original positions, or 2) coordinate extrema can be created or eliminated artificially by the tessellation (i.e. the one-to-one correspondence can be violated). Figure 3 illustrates the common error types that can occur when tessellating a complex figure on a coarse grid.

First note extremum y^6 in Figure 3. Since it occurs at a convexity, and it lies exactly on

a horizontal grid line, it will be mapped to an equivalent extremum in the tessellated figure (on the right). However, tessellation of the figure causes errors in all of the other extrema.

1.6.2. Type 1 errors

The most common type of error is seen at extremum y^1. Here, at a convexity, the extremum will be shifted up to the nearest horizontal line. This will cause an error of at most s, the height of a pixel in the grid. The maximum value of these errors can always be reduced to s^* by reducing the pixel size of the grid to s^*.

At y^5, a concave extremum on the figure, the shift in the extremum due to tessellation can be arbitrarily large, depending upon the depth of the invagination in the figure. In this case, the extremum is shifted exactly one pixel height. These errors can usually be reduced by reducing pixel size, but they are a function of both the width of the "hole" in the figure and the pixel size, so it is difficult to put a bound on these errors in terms of simple parameters of the figure.

1.6.3. Type 2 errors

In type 2 errors, extrema are destroyed or created by the tessellation. Consider the extrema y^2 and y^3 of Figure 3. The vertical extrema are so close together vertically, that they will be lumped together in the tessellated figure, effectively eliminating both of them as extrema. These errors can be avoided if the grid pixel size is smaller than the minimum horizontal or vertical distance between extrema.

Finally, consider the invagination of the figure marked by the sequence of extrema x^2, x^3, y^7, and y^8. Due to the narrowness of the gap between the two parts of the figure at this point, the tessellation will create a topological change in the figure. This topological change creates new extrema at the position of the asterisk in the tessellated figure at right. This can cause large errors in the LCAP perimeter estimate. Latecki [10] described the precise circumstances under which tessellation can produce topological errors. Choosing a pixel size small enough to avoid these conditions will alleviate these errors.

To summarize, in a practical situation one should choose the size of the tessellating pixels so that continuous coordinate extrema are mapped to their discrete counterparts in a one-

to-one manner and "sufficiently well" for the problem at hand. It may not always be clear how small the tiles need to be for a highly convoluted figure or surface. Thus, the practical application of LCAP should be limited to situations in which it is known or at least expected that the extrema are not greatly disturbed by the tessellation. For example, for the class of convex plane figures, it is easy to see that the LCAP estimate is within $8s$ of the ALCAP estimate, where s is the pixel size for the grid. Hence for this class of figures, to obtain an LCAP estimate within ε of the ALCAP estimate we must choose a pixel size so that $8s < \varepsilon$ or $s < \frac{\varepsilon}{8}$.

Having expounded the limitations of LCAP perimeter estimates, we now turn our attention to the analysis of ALCAP methods on various grids.

2. Two Dimensional Tilings

As mentioned above, we will analyze the square, hexagonal, and triangular tilings. The hexagonal tiling is unique up to rotation, but for the square and triangular tilings, different grids can be produced by shifting rows of tiles. We analyze the grids show in Figures 4A and 4B.

2.1. The Cartesian Square Tiling

Let $L_S(\theta)$ be the estimated length of a unit length line segment at angle θ computed using ALCAP on a square grid. For a unit length line segment on an infinitely fine square grid, we have

$$L_S(\theta) = |\sin\theta| + |\cos\theta| \tag{8}$$

(which is also the city block distance between the endpoints of the line segment).

Then to compute the expectation of the estimated length over our distribution $\mathcal{P}$ of random line segments, we integrate the estimated length (Eq. (8)) over the interval $[0, \pi/2]$

and divide by the interval of integration (see [8],[20]):

$$E_{\mathcal{P}}\left[L_S\left(\theta\right)\right] = \int_0^{\frac{\pi}{2}} L_S\left(\theta\right) p\left(\theta\right) d\theta = \int_0^{\frac{\pi}{2}} L_S\left(\theta\right) \frac{1}{\frac{\pi}{2}} d\theta = \frac{4}{\pi}, \tag{9}$$

We call this value the *mean length estimate* on a square grid.

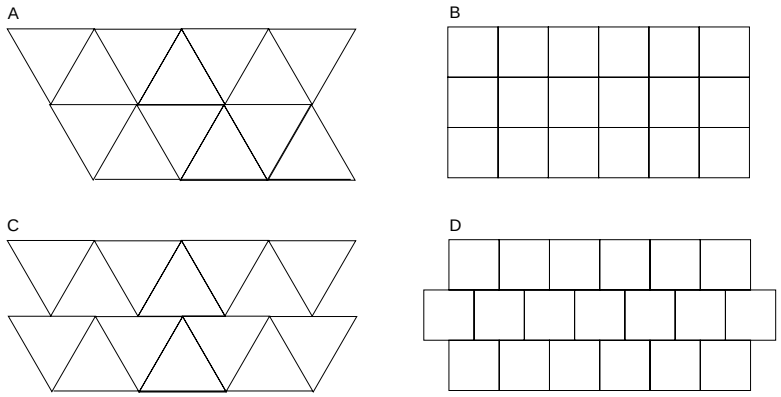

Figure 4: Some square and triangular grid variations. Only grid types A and B are analyzed in this paper. Hexagons admit only a single grid type.

On average, we overestimate the length of a line by a factor of $4/\pi \approx 1.273$ by using the city block estimate of length. We define the *length error*, which is just the difference between the true length of the line segment (which is defined to be 1) and the estimated length to be

$$e_{L_S}\left(\theta\right) = \left|L_S\left(\theta\right) - 1\right|. \tag{10}$$

Then the *expected length error*, or simply the *length bias*, is

$$E_{\mathcal{P}}\left[e_{L_S}\left(\theta\right)\right] = E_{\mathcal{P}}\left[\left|L_S\left(\theta\right) - 1\right|\right] = E_{\mathcal{P}}\left[L_S\left(\theta\right)\right] - 1 = \frac{4}{\pi} - 1 \approx 0.273. \tag{11}$$

By symmetry, we can see that the length bias will be the same for lines whose defining orientation angle lies in the other three quadrants, so the same result is obtained whether we integrate over the full range of angles or merely in the first quadrant. Notice also that we could have limited the integration to the range $\theta \in [0, \pi/4]$ since the integrated functions are symmetric about the line $\theta = \pi/4$. In fact, any of the regions shown in Figure 5A serve as a basis for the interval of integration for Eq. (9).

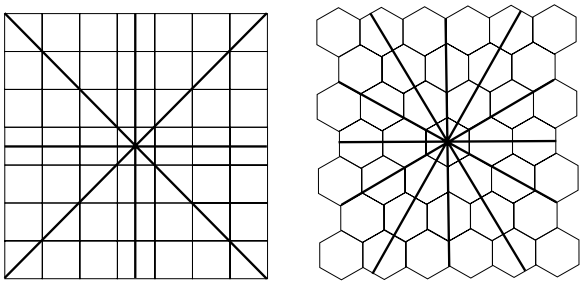

Figure 5: Bias symmetry regions for square and hexagonal tessellations. The recognition of such regions simplifies bias computations in more complicated tessellations. (The symmetry regions for the triangular grid are equivalent tot those for the hexagonal grid.)

2.2. Hexagonal Tilings

Next consider the errors obtained when the plane is tiled with hexagons, as in Figure 6. We start by noticing that for lines of unit length which lie at an angle $\theta \in [0, \pi/6]$, the following formula for estimated length holds:

$$L_H(\theta) = \frac{4}{3}\cos\theta. \tag{12}$$

The conclusion is that only the run, and not the rise, of such a line is relevant to the computation of its estimated length. To see this, note that each line which lies in the interval $\theta \in [0, \pi/6]$ (L1 and L2 in Figure 6) can be estimated by the hexagonal grid pieces in Figure 7. Each of these pieces is 4/3 as long as the distance between pixel centers along the x-axis, resulting in Eq. (12). These hexagonal grid pieces are analogous to the east-west and north-south segments used for computing city block distance on a square grid. By symmetry again, the interval $\theta \in [0, \pi/6]$ is large enough to define all the needed properties of the hexagonal tiling.

For our mean estimated length, then we have

$$E_{\mathcal{P}}[L_H(\theta)] = \int_0^{\frac{\pi}{2}} L_H(\theta)\, p(\theta)\, d\theta = \int_0^{\frac{\pi}{2}} L_H(\theta)\, \frac{1}{\frac{\pi}{2}} d\theta = \frac{4}{\pi}. \tag{13}$$

Remarkably, this is the same mean length estimate as for the square. And the *hexagonal*

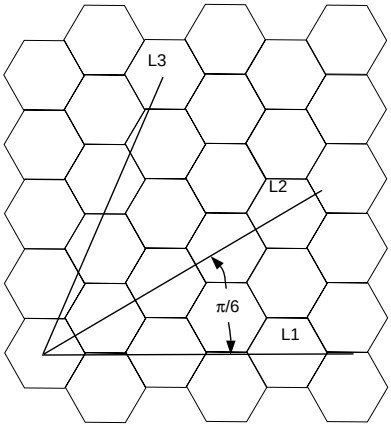

Figure 6: Lines on a hexagonal grid. For lines which lie at an angle between $\theta \in [0, \pi/6]$ radians from the x-axis, the estimated length is a constant times the length of the line projected onto the x-axis.

Figure 7: These two sections of the hexagonal grid, laid end to end, can be used to approximate any line segment which forms an angle $\theta \in [0, \pi/6]$ with the x-axis.

length bias is:

$$E_{\mathcal{P}}\left[e_{L_H}(\theta)\right] = E_{\mathcal{P}}\left[|L_H(\theta) - 1|\right] = E_{\mathcal{P}}\left[L_H(\theta)\right] - 1 = \frac{4}{\pi} - 1 \approx 0.273. \tag{14}$$

2.3. Length Bias vs. Centered Length Bias

At first glance, one might conclude that the hexagonal tiling is no better than the square tiling, since they have the same length biases. However, we can make an improvement to our estimated length function on each grid by noticing that the estimated length is almost always an overestimate of the true length. We define a new function of the line segment-valued random variable $\mathcal{P}$ called the *centered estimated length* which we define for a square grid as:

$$L_S^{cent.}(\theta) = \frac{\sin\theta + \cos\theta}{K_S}, \tag{15}$$

where K_S is a correction factor for the overestimate.

The *centered length error* is then

$$e_{L_S^{cent.}}(\theta) = \left| \frac{\sin\theta + \cos\theta}{K_S} - 1 \right|, \tag{16}$$

such that, for appropriate values of K_S (a little bit larger than 1), $e_{L_S^{cent.}}$ should have a lower mean value than the previously defined error measure. That is, by assuming that the true length of a line segment is a little bit less than the value actually obtained from the local counting algorithm, we are likely to be closer to the true line segment length. The *expectation of the centered length error* is:

$$E_{\mathcal{P}}\left[e_{L_S^{cent.}}(\theta)\right] = \int_0^{\frac{\pi}{2}} \left| \frac{\sin\theta + \cos\theta}{K_S} - 1 \right| \frac{1}{\frac{\pi}{2}} d\theta, \tag{17}$$

which we call the *centered bias* for the square tiling. We define K_S to be the value which minimizes this expectation. K_S is difficult to obtain analytically due to the absolute value within the integral. However, evaluating numerically using a commercial math package [22], we obtain $K_S \approx 1.323$, and $E_{\mathcal{P}}\left[e_{L_S^{cent.}}(\theta)\right] \approx 0.0798$, implying that even after centering, we can expect an error of approximately 8 percent in the length of lines or the perimeter of a figure on a square grid. Summarizing, the integral above represents the mean magnitude of the difference between the true length of the line, which we have defined to be 1, and the centered estimated length.

On a hexagonal grid, the expectation of the centered estimated length becomes

$$E_{\mathcal{P}}\left[e_{L_H^{cent.}}(\theta)\right] = \int_0^{\frac{\pi}{6}} \left| \frac{\frac{4}{3}\cos\theta}{K_H} - 1 \right| \frac{1}{\frac{\pi}{6}} d\theta. \tag{18}$$

Here, through numerical methods again, we obtain $K_H \approx 1.291$, and $E_{\mathcal{P}}\left(L_H^{cent.}(\theta)\right) \approx 0.0348$. Hence, tiling with hexagons does improve the mean accuracy of length estimates by almost five percent over the square tiling.

2.4. Triangular Tilings

We also evaluated an equilateral triangular tiling. The mean length estimate for the triangular tiling was superior to the other tilings, giving a length bias ≈ 0.103.

However the centered bias and the squared centered bias matched exactly the values for the hexagonal tiling. This can be explained by the fact that each path on an hexagonal grid is a constant factor longer ($\frac{2}{\sqrt{3}}$ than the corresponding path on a triangular grid, provided the grids are at a certain orientation). Since the centered bias and the squared centered bias are computed by minimizing over a factor which divides the length, the constant factor which accounts for the difference between the two tilings is eliminated.

2.5. Error Extrema and the Squared Centered Bias

Before moving on to 3-D tessellations, we examine a few more statistics for two-dimensional tilings, the error extrema and the squared centered bias.

Table 1 shows the maximum and minimum errors both before and after centering for the three tilings. Notice that the maximum centered error for the triangular tiling is less than half of that for the square tiling and is about 20 percent less than for the hexagonal tiling. Hence, in any application where maximum error is critical, tessellating with a triangular grid may be worth the trouble.

2.5.1. Squared centered bias

An alternative to the centered error discussed previously involves weighting large errors more heavily than small errors. To do this we can merely square the residue used in previous expressions. This gives us

$$e_{L_S^{sq.}}(\theta) = \left(\frac{\sin\theta + \cos\theta}{K_S} - 1\right)^2, \tag{19}$$

for the square grid, with an expectation of

$$E_{\mathcal{P}}\left[e_{L_S^{sq.}}(\theta)\right] = \int_0^{\frac{\pi}{2}} \left(\frac{\sin\theta + \cos\theta}{K_S} - 1\right)^2 \frac{1}{\frac{\pi}{2}} d\theta, \tag{20}$$

	Triangle		Square		Hexagon	
Statistic	**Closed Form**	**Approx.**	**Closed Form**	**Approx.**	**Closed Form**	**Approx.**
Mean Length Estimate	$\frac{2\sqrt{3}}{\pi}$	1.103	$\frac{4}{\pi}$	1.273	$\frac{4}{\pi}$	1.273
Maximum Error	$\frac{2\sqrt{3}}{3}-1$	0.155	$\sqrt{2}-1$	0.414	$\frac{1}{3}$	0.333
Minimum Error	0	0.0	0	0.0	$\frac{2\sqrt{3}}{3}-1$	0.155
Length Bias	$\frac{2\sqrt{3}}{\pi}-1$	0.103	$\frac{4}{\pi}-1$	0.273	$\frac{4}{\pi}-1$	0.273
Optimal Centering Constant	–	1.118	–	1.323	–	1.291
Maximum Centered Error	–	0.106	–	0.244	–	0.134
Minimum Centered Error	0	0.0	0	0.0	0	0.0
Centered Bias	–	0.0348	–	0.0798	–	0.0348
Squared Centered Bias	$\frac{2\pi^2+3\sqrt{3}\pi-36}{\pi\left(3\sqrt{3}+2\pi\right)}$	0.00176	$\frac{\pi^2+2\pi-16}{\pi(\pi+2)}$	0.00946	$\frac{2\pi^2+3\sqrt{3}\pi-36}{\pi\left(3\sqrt{3}+2\pi\right)}$	0.00176

Table 1. Some estimated-length statistics of a random unit-length line segment process under triangular, square, and hexagonal tessellations. For non-centered length bias, the triangular grid is the winner. After centering, however, the triangular and hexagonal grids perform equally well, both signficantly outperforming the square grid.

which we call the *squared centered bias*.

The value which minimizes the above equation (K_S) represents the "best" adjustment of our guess at the true length of the line given that we want to weigh larger errors more heavily. Values for the squared centered bias are given for the three two-dimensional tilings in Table 1.

3. Three Dimensional Tilings

We now turn to the problem of estimating the surface area of a volume on a discrete grid in three dimensions using ALCAP. The basic procedure is for each voxel to report the amount of its own surface area which is part of the surface area of the global object. Measurements of surface area will be biased again due to the discretization of the volume. We replace our unit length line segment process $\mathcal{P}$ from 2-D with a unit area *planar patch* process $\mathcal{Q}$ in 3-D.

In two dimensions, we examined regular polygons which can tile the plane. Unfortunately, there is only a single regular polyhedron, the cube, which can tile 3-space. Looking for alternatives to cubes with as many symmetries as possible, we expanded our search to two additional groups, the semi-regular polyhedra and their duals. Lyusternik [14, page 147] defines a semi-regular polyhedron as "a polyhedron all of whose faces are regular polygons (though all faces need not be of the same type) and all of whose polyhedral angles are equal." Properties of these solids and the regular polyhedra can be found in [4, 14, 21].

Exactly one semi-regular polyhedron, the truncated octahedron, tiles space. It is pictured in Figure 11. And exactly one dual of the regular and semi-regular polyhedra, the rhombic dodecahedron, tiles space. (See Figure 16). It is the dual of the cuboctahedron, another semi-regular polyhedron. As an initial effort, we limit the scope of this paper to these two solids and the cube. However, it would be interesting in future work to find the optimal tiling solid for surface area computations.

3.1. Cubic Tilings

Let θ and ϕ define the normal to a planar segment, as one would define a point on the unit sphere by two angles. Such a patch and the associated angles can be seen in Figure 8. The

estimated area of this planar segment using ALCAP on a cubic grid is then:

$$A_C(\theta, \phi) = \sin\phi + \cos\phi\cos\theta + \cos\phi\sin\theta. \tag{21}$$

The three terms on the right hand side of Eq. (21) are the projections of the planar segment

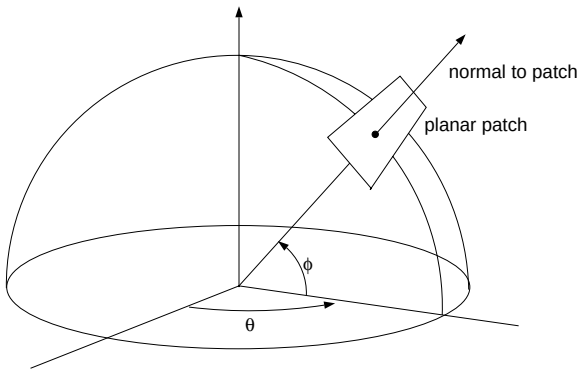

Figure 8: A planar patch and its associated angles.

onto each of the primary Cartesian planes (x-y, y-z, x-z) respectively. This projection process is analogous to finding the city block length estimate in two dimensions.

3.1.1. Expected Estimated Area

Integrating Eq. (21) over the angles θ and ϕ in the interval $[0, \pi/2]$ and dividing the result by the solid angle (in units of steradians) over which we have integrated gives us the *mean area estimate* or *expected area estimate* obtained with a cubic grid over $\mathcal{Q}$. We need to multiply the area expression by the Jacobian term, $\cos\phi$, which handles the foreshortening of area as we approach the "north pole" of the unit sphere. We have

$$E_{\mathcal{Q}}\left[A_C(\theta, \phi)\right] = \frac{\int_0^{\frac{\pi}{2}}\int_0^{\frac{\pi}{2}} A_C(\theta, \phi)\cos\phi\, d\phi\, d\theta}{\int_0^{\frac{\pi}{2}}\int_0^{\frac{\pi}{2}} \cos\phi\, d\phi\, d\theta} = \frac{\int_0^{\frac{\pi}{2}} \frac{1}{2} + \frac{\pi}{4}(\sin\theta + \cos\theta)\, d\theta}{\int_0^{\frac{\pi}{2}} 1 d\theta} = \frac{\frac{\pi}{4} + \frac{\pi}{2}}{\frac{\pi}{2}} = \frac{3}{2}. \tag{22}$$

In the case of calculating the mean length estimate on a square grid in two dimensions, we noted that we could restrict our interval of integration to $\theta \in [0, \pi/4]$, due to the symmetry of a square grid. There is an analogous, albeit more complicated symmetry in 3-D on a

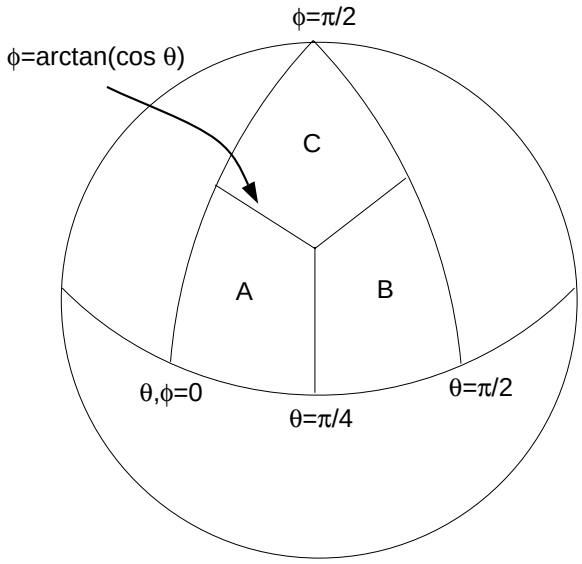

Figure 9: Integrating the estimated area expression in Eq. (21) over the spherical triangle shown $\theta \in [0, \pi/2]\,; \phi \in [0, \pi/2]$ yields the area bias for planar segments on a cubic grid. We obtain the same result if we restrict the solid angle of integration to Area A, B, or C (area A is used in the text).

cubic grid. Picture a sphere whose center is at the origin and whose equator lies in the x-y plane, as in Figure 9. The family of planar segments whose normals fall within the solid angle of Area A (or B or C for that matter) of Figure 9 have the same estimated areas and hence the same mean estimated area as the total family of planar segments whose normals lie in a single Cartesian octant. That is, just as the range $\theta \in [0, \pi/4]$ represents all of the unit length line segments needed to calculate the mean estimated length on a square grid, the part of the unit sphere defined by $\theta \in [0, \pi/4]\,; \phi \in [0, \arctan(\cos\theta)]$ represents a family of unit area planar segments sufficient to calculate the mean estimated area on a cubic grid. To understand this, note that the function we are evaluating (from Eq. (21)) is symmetric with respect to the three coordinate axes. That is, if we relabel the axes and their associated angles, the value of the function integrated across the entire region remains the same. (Actually, the smallest possible regions of symmetry are half the size of those shown in Figure 9. One can subdivide each of the Regions A, B, and C into smaller regions by drawing a great circle across the sphere from the center of the lune to the corner of the lune. This gives a total of six regions of symmetry per spherical octant, for a total of 48 regions of symmetry on the sphere. The six part symmetry is particularly apparent in Figure 10E and

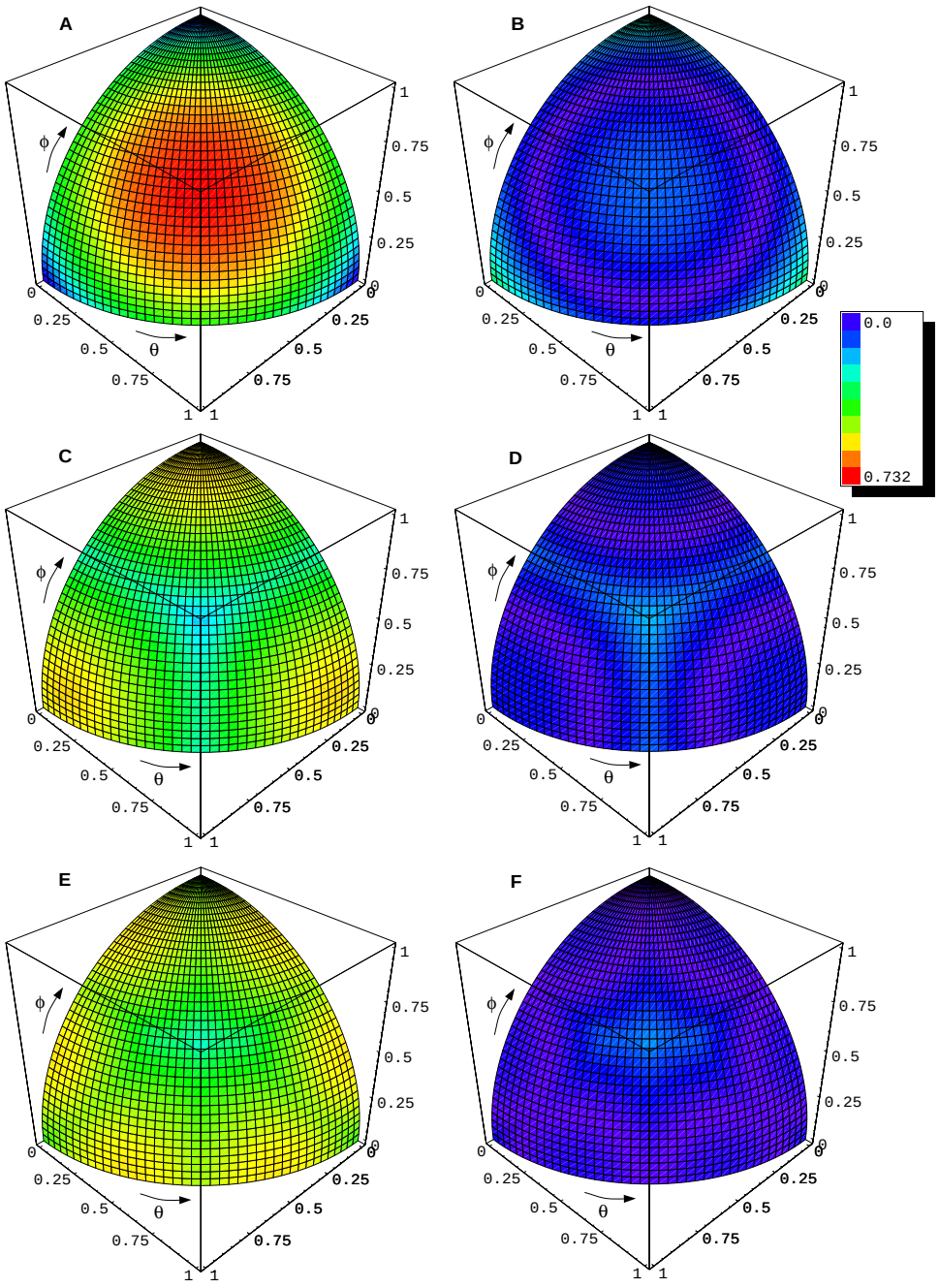

Figure 10: Estimated area error and centered estimated area error as a function of surface angle for different tessellations. **A.** Estimated surface area error for the cubic tiling. Notice that the errors are zero at the corners of the lune, which represent the errors for planes parallel to the three principal Cartesian planes. The mean error is large, however. **B.** The centered area error for cubes. The mean error is greatly reduced by centering the error. **C.** Surface area error for a TO tiling. Notice that the maximum error is reduced but the minimum error is increased. **D.** The centered surface area error for the TO tiling. **E.** Surface area error for the RD tiling. Notice the low variance in the error. **F.** Centered surface area error for the RD tiling. This tiling achieves the least centered area bias of the tilings we analyzed.

Figure 10F.) This concept can be verified by integrating the equation for area bias over 1/3 of the spherical triangle shown in Figure 9, i.e. the solid angle which is represented by Area A. We should end up with the same mean area estimate which was computed in Eq. (23), namely, 3/2. We see that this is in fact the case:

$$\frac{\int_0^{\frac{\pi}{4}} \int_0^{\arctan(\cos\theta)} A_C(\theta,\phi)\cos\phi\, d\phi\, d\theta}{\int_0^{\frac{\pi}{4}} \int_0^{\arctan(\cos\theta)} \cos\phi\, d\phi\, d\theta} = \frac{\frac{\pi}{4}}{\frac{\pi}{6}} = \frac{3}{2}. \tag{23}$$

This symmetry provides us with a slew of identities which can be found in Appendix A. These identities are helpful in deriving closed form solutions to area bias estimates for more complicated tilings which we shall encounter later.

3.1.2. Area Bias, Centered Area Bias, and Other Statistics

Once we have established the area estimation function and calculated the mean area estimate for a tiling, the computations of other statistics for that tiling follow straight forwardly. While it is not always easy to obtain a closed form solution for these statistics, at least numerical approximations can be obtained.

Since we described in detail the various statistics chosen for the 2-D tilings, we omit repeating our exposition of these statistics for the cubic tiling, and merely present formulas and solutions for the additional statistics below. These results are summarized in Table 2.

Area Bias for Cubic Tiling. We define the *area error* to be

$$e_{A_C}(\theta,\phi) = |A_C(\theta,\phi) - 1|, \tag{24}$$

and the expectation of this quantity, or *area bias*, is then

$$E_{\mathcal{Q}}[e_{A_C}(\theta,\phi)] = E_{\mathcal{Q}}[|A_C(\theta,\phi) - 1|] = E_{\mathcal{Q}}[A_C(\theta,\phi)] - 1 = \frac{3}{2} - 1 = 0.5. \tag{25}$$

Figure 10A shows the area error for a cubic tiling as a function of θ and ϕ, the two angles which define the normal to a planar segment. The color at each point represents the error

	Cube		Truncated Octahedron		Rhombic Dodecahedron	
Statistic	**Closed Form**	**Approx.**	**Closed Form**	**Approx.**	**Closed Form**	**Approx.**
Mean Area Estimate	$\frac{3}{2}$	1.500	$\frac{3}{8} + \frac{9\sqrt{6}}{4\pi}\arctan\frac{1}{\sqrt{2}}$	1.455	$\frac{3}{2}$	1.5
Maximum Error	$\sqrt{3}-1$	0.732	$\frac{\sqrt{30+6\sqrt{3}}}{4} - 1$	0.589	$\frac{\sqrt{10}}{2} - 1$	0.581
Minimum Error	0	0.0	$\frac{\sqrt{3}-1}{4}$	0.183	$\sqrt{2}-1$	0.414
Area Bias	$\frac{1}{2}$	0.500	$-\frac{5}{8} + \frac{9\sqrt{6}}{4\pi}\arctan\frac{1}{\sqrt{2}}$	0.455	$\frac{1}{2}$	0.5
Optimal Centering Constant	–	1.533	–	1.478	–	1.517
Maximum Centered Error	–	0.348	–	0.191	–	0.0701
Minimum Centered Error	0	0.0	0	0.0	0	0.0
Centered Bias	–	0.0812	–	0.0580	–	0.0318
Squared Centered Bias	–	0.0102	–	0.00462	–	0.00191

Table 2. Some statistics for random plane processes on tessellations of cubes, truncated octahedra, and rhombic dodecahedra.

for the planar segment defined by that particular point. For the cubic tiling, as expected, the error is zero at the three corners of the plot, since this corresponds to the three principal Cartesian planes, which can be perfectly represented in a cubic tiling. However, as the angle of the plane becomes more oblique, the error increases quickly. The maximum error occurs in the middle of the plot and has an area error of $\sqrt{3} - 1 \approx 0.732$. Figure 10B shows the benefit of centering the error which is discussed in the following section.

Centered Bias for Cubic Tiling. To produce the *centered area bias*, we must first define the *centered estimated area* to be

$$A_C^{cent.}(\theta, \phi) = \frac{A_C(\theta, \phi)}{K_C}, \tag{26}$$

where K_C is the correction factor for the overestimate of area. Then, the *centered area error* is:

$$e_{A_C^{cent.}}(\theta, \phi) = \left| \frac{A_C(\theta, \phi)}{K_S} - 1 \right|, \tag{27}$$

and the expectation of this quantity is just

$$E_{\mathcal{Q}}\left[e_{A_C^{cent.}}(\theta, \phi)\right] = \int_0^{\frac{\pi}{4}} \int_0^{\arctan(\cos\theta)} \left| \frac{A_C(\theta, \phi)}{K_C} - 1 \right| \frac{1}{\frac{\pi}{6}} \cos\phi \, d\phi \, d\theta. \tag{28}$$

Minimizing over K_C using numerical methods, we obtain $K_C \approx 1.533$ corresponding to a *centered area bias* of approximately 0.0812. Figure 10B shows a plot of the centered area error as a function of the planar segment normals. Notice the greatly reduced error due to the correction factor.

Squared Centered Bias for Cubic Tiling. Following in the same vein, we compute the *squared centered error* for area, as

$$E_{\mathcal{Q}}\left[e_{A_C^{sq.}}(\theta, \phi)\right] = \int_0^{\frac{\pi}{4}} \int_0^{\arctan(\cos\theta)} \left(\frac{A_C(\theta, \phi)}{K_C} - 1 \right)^2 \frac{1}{\frac{\pi}{6}} \cos\phi \, d\phi \, d\theta, \tag{29}$$

The value of $K_C \approx 1.516$ minimizes the expression, which has a corresponding value of approximately 0.0102.

Error Maxima and Minima for Cubic Tiling. In two dimensions, computing the values of θ which maximized and minimized our estimated length functions was easy since these functions are monotonic over the relevant range of θ. In three dimensions, this same statement holds for the partial derivatives (with respect to ϕ and θ) of the cubic grid estimated area function, so again we have it easy:

$$\max_{\theta,\,\phi} A_C(\theta,\phi) = A_C\left(\frac{\pi}{4}, \arctan\left(\cos\frac{\pi}{4}\right)\right) = \sqrt{3}, \tag{30}$$

and

$$\min_{\theta,\,\phi} A_C(\theta,\phi) = A_C(0,0) = 1. \tag{31}$$

These values give us a maximum centered error of approximately 0.348, and the minimum centered error is of course 0.

3.1.3. Summary of Results for Cubic Grid

The expected error when we simply compute area of a smooth figure on a cubic grid using a local counting scheme is exactly 50 percent. While this is large, we can do substantially better by dividing the ALCAP result by 1.533 and using this as our guess of the true area. Our expected error is then only about 8 percent. However, as we shall see, we can do substantially better than this by using other grids. Furthermore, our worst case error, even after centering, is still 34 percent, which is quite severe for some applications. This too, we would like to improve upon.

3.2. The Truncated Octahedron

A simple solution finding the ALCAP surface area estimates for a truncated octahedron (TO) grid relies on finding certain symmetries in the tiling which we can exploit.

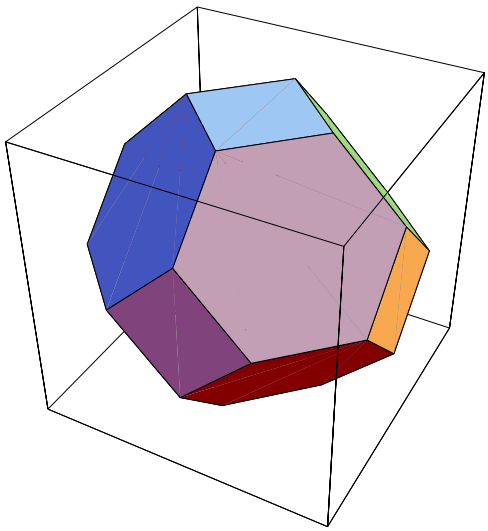

Figure 11: A truncated octahedron.

3.2.1. The Estimated Area Function for Truncated Octahedral Grids

Unlike the square, the cube, and the hexagon, it is not immediately obvious how to align the TO's with respect to the coordinate axes to simplify our analysis of estimated surface area. Figure 12 shows several possibilities, assuming the viewer is looking down along the z-axis, from a point P at $(0, 0, 1)$. The one shown on the far right is of particular interest, since it is symmetric with respect to the three coordinate axes. That is, in this orientation, the TO would look exactly the same if projected onto any of the three principal Cartesian planes. This feature greatly simplifies the computation of the estimated area of a planar segment tiled with TO's.

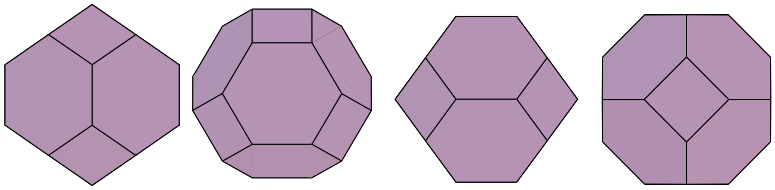

Figure 12: Four views of a truncated octahedron. The choice of orientation of this solid relative to the coordinate axes can significantly affect the complexity of the analysis of surface area bias. Because it is symmetric with respect to the three coordinate axes, the orientation shown in the rightmost drawing is used in this paper.

Another key property of this particular orientation of the TO is that for the discretization of a plane which forms an angle of less than $\pi/4$ with the x-y plane (exactly those planes

whose normals lie in Region C of Figure 9), if we view the tiling from the z-axis, that is, from a point P at $(0, 0, 1)$, *we can see every voxel (but not necessarily every exposed facet of each voxel) which is part of the surface representation.* That is, the projection of the surface onto the x-y plane contains part of every voxel which is part of the surface representation. That is, there are no "hidden voxels" as there would be for the representation of planes at steeper angles, or with different orientations. This projection will always look something like the diagram in Figure 13. In particular, all of the exposed hexagonal facets will be visible, and all of the square facets which are parallel to the x-y plane will be visible. This is critical in that it allows us to count the contribution to area made by these faces from a projection of the tessellated plane.

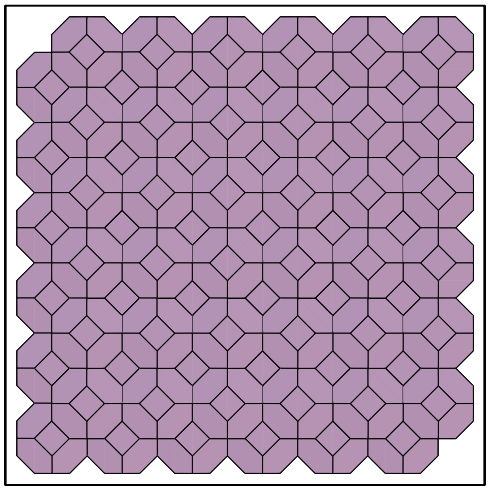

Figure 13: A part of a surface represented with truncated octahedra as described in the text. The view is from any of the coordinate axes.

To get a better understanding of this phenomenon, examine Figure 14. This represents the intersection of a TO tiling of a planar surface with the x-z plane. Notice that the angle $\theta < \pi/4$. The viewer from above will always be able to see each voxel which is part of the surface. In fact, the projection of this surface contains an image of every facet of each voxel which is part of the planar representation, except for those facets marked as "invisible". Additional insights may be gained by referring to Figures 15A, which shows a planar patch tessellated with truncated octahedra, and Figures 15B, C, and D, which show approximate projections of the patch onto the three Cartesian planes.

If we were only interested in the surface facets which were viewable from this angle, we

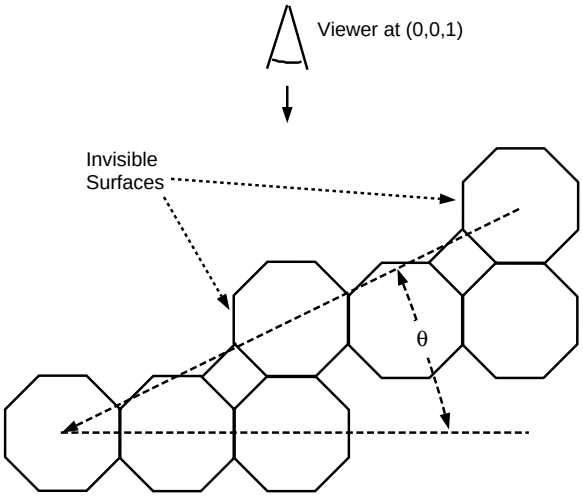

Figure 14: Intersection of TO tiling of a surface with the x-z plane. Notice that while all voxels which are part of the surface can be seen from above, not all facets of those voxels which contribute to the surface area can be seen.

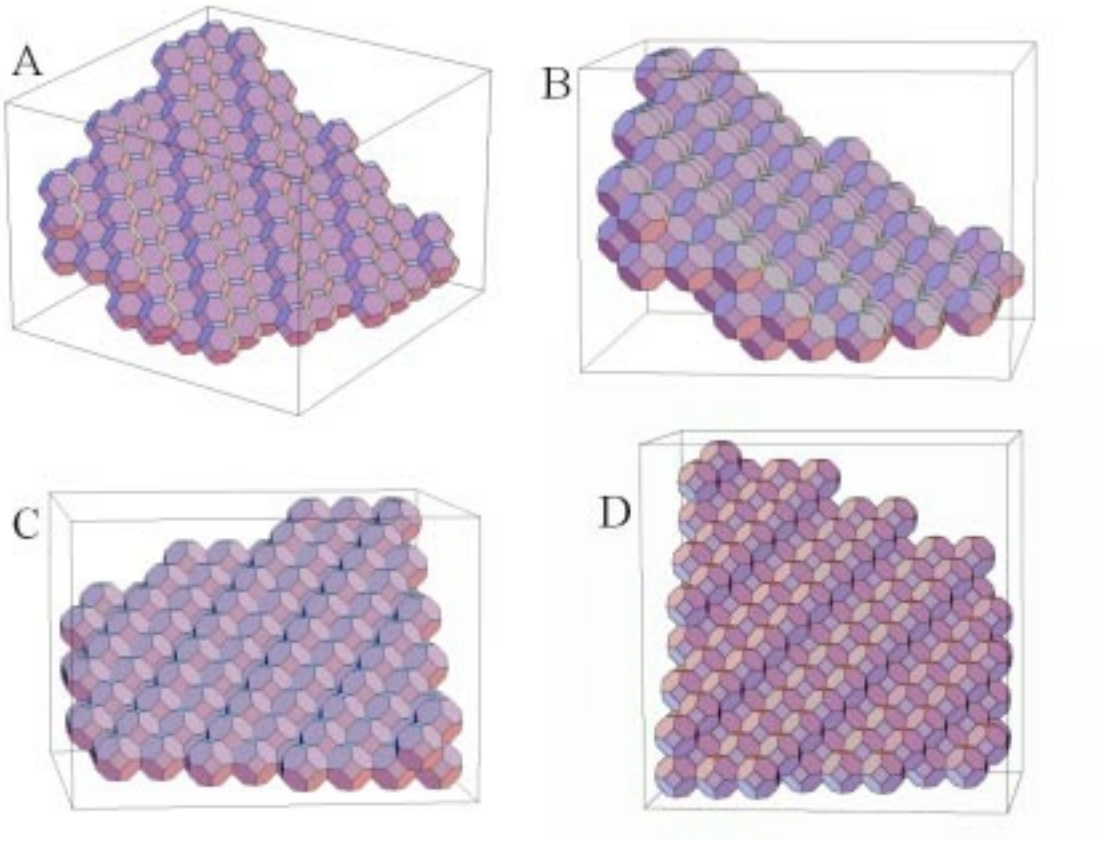

Figure 15: Views of a planar patch which has been tessellated with truncated octahedra. **A.** An oblique view of the patch. **B, C, D.** Three nearly perpendicular projections of the patch.

could compute their area with the formula

$$A_{T_{xy}}(\phi,\theta) = \left(\frac{1}{4} + \frac{3}{4}\sqrt{3}\right)\sin\phi \tag{32}$$

since 1/4 of the projected area is covered by square faces of TO's whose projected areas are equivalent to their original areas and 3/4 of the projected area is covered by hexagonal faces of TO's which have been foreshortened by a factor of $\sqrt{3}$. However, this approach would miss the "invisible facets" shown in Figure 14. To compute their contribution to the surface area of the tessellated surface, we must view the surface from both the x- and y-axes as well. That is, we must project the surface onto both the y-z and the x-z planes and add area from these projections to the estimated area expression.

Adding together these three projections without modification will over-count the area, however, since the hexagonal facets which appear in the y-z and x-z projections also appear in the x-y projections. We do not want to count any facet more than once. Hence, we only count the portion of the projection which resulted from projecting the square facets for our second and third projections. This gives the formula:

$$A_T(\phi,\theta) = \left(\frac{1}{4} + \frac{3}{4}\sqrt{3}\right)\sin\phi + \frac{1}{4}\sin\theta\cos\phi + \frac{1}{4}\cos\phi\cos\theta, \quad \{\forall\,(\phi,\theta) \in C\}, \tag{33}$$

where C again represents Region C of Figure 9.

This formula is only valid because we are limiting our analysis to planes which form an angle of less than $\pi/4$ with the x-y plane. The best analogy here is again with the analysis of perimeter on a hexagonal grid in two dimensions. On a hexagonal grid, the simple formula for perimeter only holds for certain sets of line segments, those which form an angle of less than $\pi/6$ with the x-axis.

Now that we have an expression for the estimated area at a particular pair of angles, θ and ϕ, we can integrate our expression for estimated area (A_T) over the appropriate solid angle interval, again using the proper Jacobian, to obtain the mean estimated area for a TO tiling:

$$E_{\mathcal{Q}}\left[A_T(\phi,\theta)\right] = \frac{\iint_C A_T(\phi,\theta)\cos\phi\,d\phi\,d\theta}{\iint_C \cos\phi\,d\phi\,d\theta} = \frac{\frac{\pi}{16} + \frac{3\sqrt{6}}{8} \times \arctan\frac{1}{\sqrt{2}}}{\frac{\pi}{6}} \approx 1.455. \tag{34}$$

(For a more detailed exposition of this result, refer to Appendix B.)

3.2.2. Other Statistics on the TO Grid

As with the cubic tiling, it is interesting to examine a variety of statistics for the TO tiling. Since these are computed in a manner identical to that of the cubic tiling, they are simply summarized in Table 2. The most significant item to note in the table regarding the TO is that the centered area bias is significantly lower for the TO grid. This means we can estimate the area of an arbitrary binary volume significantly more accurately using a local counting algorithm on a TO grid than on a cubic grid. This is a very satisfying result. However, we may be able to do better yet!

3.3. The Rhombic Dodecahedron

Finally, we examine one last solid, the rhombic dodecahedron. Several of its projections onto planes are identical to the projections of cubes, and hence from some angles, it looks exactly like a cube. This can be very confusing to the eye. Nevertheless, it does tile space, and we examine its properties here.

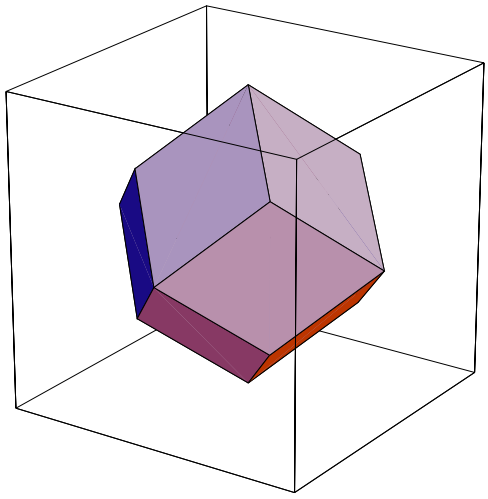

Figure 16: The rhombic dodecahedron.

3.3.1. The Estimated Area Function for Rhombic Dodecahedral Grids

As was the case for truncated octahedra, it turns out to be useful for the purposes of tessellation analysis to look for symmetries in the rhombic dodecahedron (RD) relative to the coordinate axes. The RD also has a 3-D orientation such that the projection onto each of the three major Cartesian planes is equivalent. Figure 17 shows possible candidates for tiling orientations, and the orientation on the right has the desired property, i.e. it looks the same to a viewer from any of the coordinate axes.

Recall that for a TO tiling, all voxels which contributed to the surface area computation of a tessellated plane were at least partially visible from the z-axis. Also all of the facets which were not perpendicular to the line of sight (the "invisible facets") made a contribution to the projection of the tessellated plane onto the x-y plane. Given the above choice of orientation for RD voxels, we have the same situation for the RD grid. For a plane whose normal makes an angle of less than $\pi/4$ with the z-axis and which is tessellated with RD's, each voxel which is part of the surface of that plane can be seen when the tessellated plane is viewed from infinity on the z-axis. Figure 19 shows the appearance of such a tessellation when viewed from the z-axis. As with the TO tiling, the part of the surface area which

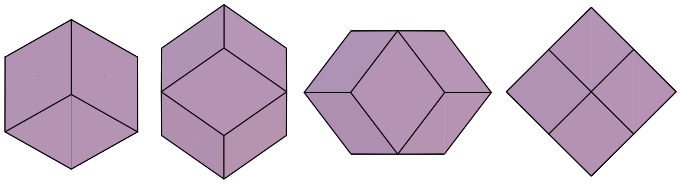

Figure 17: Projections of the rhombic dodecahedron.

can be seen from this limited perspective has a simple formula in terms of the projection of the plane. (Figure 18 offers additional renditions of a rhombic dodecahedron-tiled planar segment projected onto several different planes.) Each rhombic facet is foreshortened by $\sqrt{2}$, yielding the following formula for planar segments of unit area whose normals are designated by (ϕ, θ):

$$A_{xy}(\phi, \theta) = \sqrt{2} \sin \phi. \tag{35}$$

However, as with the case of the truncated octahedron, Eq. (35) does not capture all of the area which is part of the tessellated surface. That is, there are again certain "invisible"

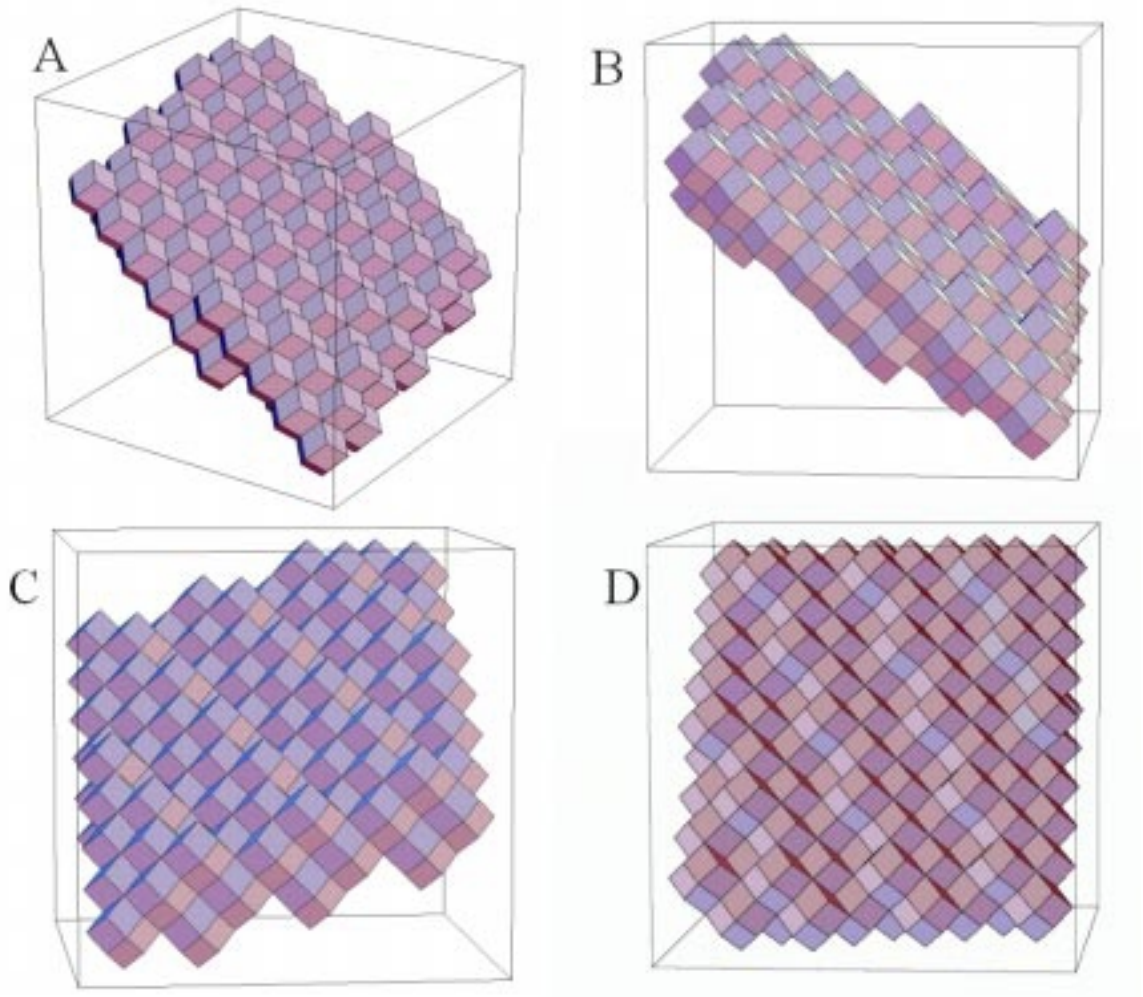

Figure 18: Views of a planar patch which has been tessellated with rhombic dodecahedra. **A.** An oblique view of the patch. **B, C, D.** Three nearly perpendicular projections of the patch.

facets which are not captured by that projection. To measure the rest of the area, we must add in parts of other projections as well. It took a bit of experimentation to find the projections which allow one to count each face only once. It turns out that if we project the surface onto the planes whose equations are $x = z$ and $y = z$, we obtain exactly twice the area of the remaining uncounted area.

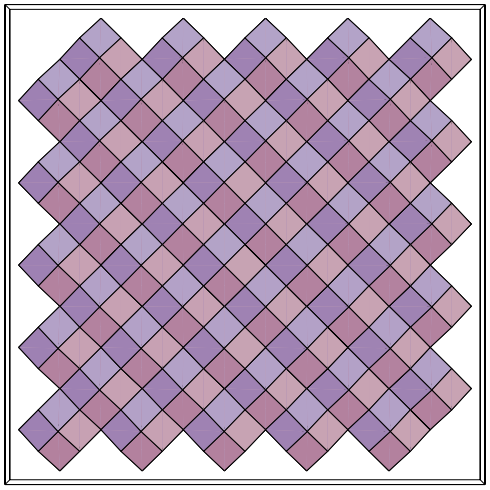

Figure 19: A surface tessellated with rhombic dodecahedra, as viewed from along the z-axis.

Hence, our new and complete formula for estimated area on the RD grid becomes

$$A_R(\phi,\theta) = \sqrt{2}\sin\phi + \frac{1}{2}\cos\phi\cos\left(\theta+\frac{\pi}{4}\right) + \frac{1}{2}\cos\phi\sin\left(\theta+\frac{\pi}{4}\right), \quad \{\forall\,(\phi,\theta)\in C_L\}, \quad (36)$$

where the last two terms are 1/2 the projection onto the aforementioned planes. This expression can also be integrated (see Appendix B) to yield the results found in Table 2. Note that the equation is accurate only over a subset of the Region C from Figure 9. We call this Region C_L since it is the left half of Region C. Fortunately, it represents another (albeit smaller) of the "symmetry regions" discussed earlier. That is, integrating over it alone produces the correct mean area error. We refer the reader again to Figures 10E and F for an illustration of these smaller symmetry regions.

3.4. Summary of Results for 3-D

Examining Table 2, we see that while the truncated octahedron gives the best result for mean area estimate, the rhombic dodecahedron has a significantly smaller centered area bias and also a much smaller maximum centered error. This is a significant result if we are trying to minimize the error in surface area computation using local counting algorithms on a regular grid.

To understand these results visually, examine Figure 10. On the left of the figure are plotted the area errors of the cubic, truncated octahedral, and rhombic dodecahedral tilings as functions of the planar segment normals. Notice that while the cube has the smallest errors of any of the plots (the error is zero at the corners of the lune), it also has the largest error (in the center). It also has a large variation in error. This implies that after centering the error, the other tessellations may do better. This is demonstrated on the right hand side of the figure, which shows the centered area error for each of the tessellations. In particular, notice that the rhombic dodecahedral centered error (F) has relatively low error throughout the plot. This gives some intuition to the result that the overall centered error bias is lower for the RD tiling.

4. Discussion and Applications

Given the results in Table 2, it is clear that the truncated octahedron and the rhombic dodecahedron tessellations produce more accurate surface area estimates for random planes as characterized by our process $\mathcal{Q}$. While the main thrust of this paper is not applications, it is worth mentioning a few possibilities here.

The justification for this work is mostly of a "basic research" nature. Surface area is one of the most fundamental properties of solid volumes, and understanding its computation under certain constraints may or may not prove fruitful. Some researchers have let their excitement about alternative tessellations in two dimensions get in the way of reason. That is, just because a tessellation has certain mathematical properties does not necessarily mean that it will be useful in a particular situation. In particular, some researchers lament the fact that virtually all modern imaging and display has been done on raster grids and displays.

They hope that there is some way to "recover" the lost data from this sampling process and make use of it on a hexagonal grid. However, the original data is already gone. We cannot create more data by "resampling" on a hexagonal grid.

For example, Her and Yuan [7] espouse the advantages of a hexagonal grid relative to a square grid of the *same resolution*. But because, as they put it, "a real hexagonal grid device is very difficult to find", they proceed to discuss the advantages of creating a pseudo-hexagonal grid by combining pairs of pixels on a square grid. This process, however, can only destroy information. The resulting images will obviously have poorer resolution, as the authors discuss. But the authors claim "in some cases, however, that better connectivity and symmetry properties in an image are no less important than the resolution itself." The only problem with this argument is that we could have obtained the exact same connectivity information directly from the original square grid without losing any information. The eagerness to apply the advantages of a new tessellation should not obscure the fact that it simply may not be worth it.

Hence, we must look for applications where the original continuous data is still available or for which hardware is not inherently rectangular, such as in raster displays. One of the most promising potential application areas which satisfies these requirements is in medical imaging.

4.1. Medical Applications

The advent of many volumetric medical imaging modalities (magnetic resonance imaging (MRI), computed tomography (CT), high resolution ultrasound imaging, etc.) have resulted in a large number of quantitative studies of 3D structures, for example see [16]. While many of these are based on volume measurements rather than surface area measurements, improving the accuracy of surface area estimates may make this measure more attractive. Petty et al. [18] studied surface area measurements of the *planum temporale* (a relatively smooth part of the brain) in schizophrenic patients as a correlate of disease. Such studies could presumably benefit from better surface area measurements, especially since analytical models of the surfaces being measured are unavailable.

Body surface area is commonly used in computing doses for various pharmaceuticals.

This measure is commonly approximated using only a patient's weight and height. It would seem that a full body scan with a subsequent surface area analysis could yield a better estimate of surface area, if this expense were warranted. At a minimum, such techniques could be used to find more accurate correlates of true body surface area.

In medical applications, the original data (human tissue properties) are for all practical purposes continuous. At some point these data must be discretized for analysis. If we cannot get access to the data before discretization, then alternative tessellations are of no use. Hence, for retrospective medical analysis, in which we only have the discretized medical images, we can think of no way to make an improvement in surface area estimates. However, MRI is acquired as frequency data and modifying the software to sample this data along a truncated octahedral grid or a rhombic dodecahedral grid may not be difficult.

4.1.1. The Practicality of Using TO and RD Voxels

At first glance, TO's and RD's appear much more complicated than cubic or rectangular prism voxels. However, many of the properties in which we are interested are not difficult to compute on these grids. For example, finding the voxel which contains a particular spatial point is just a matter of finding the nearest voxel center, since the TO and RD tessellations are both Dirichlet (Voronoi) tessellations. Also, keeping the voxels in a logically arranged order in memory may be of some concern. The realization that the centers of voxels in a TO tiling have positions equivalent to two interleaved rectangular prism grids and in an RD tiling have positions equivalent to four interleaved rectangular prism grids suggests a variety of relatively straightforward addressing schemes, such as keeping a pair of rectangular arrays for a TO tiling. We do not want to imply that there is no additional cost in using these tessellations, but only that many tasks are still manageable on these grids.

4.2. Industrial Applications

In the manufacturing world, there are a number of reasons that one may want to know the surface area of an irregularly shaped object. These include calculating flux of some physical quantity across or along a surface such as shear stress, heat or electromagnetic fields [1],

computing wind resistance (as in the automotive industry), or merely needing to know how much paint or substrate one needs to cover an object. While in some engineering situations, a manufactured device is composed of objects whose surface area is easily computable, this is not always the case [12, 13]. In these situations, application of the results presented here may be of some use.

4.3. Other Properties of the RD and TO Tilings

If the computation of surface area alone is not enough to justify a new representation for solids in a particular application, other properties of the RD and TO tilings may be enough to swing the balance.

4.3.1. Tessellation as Sampling

For example, we can view the process of voxelization in the signal processing context as a sampling. As implied by Mersereau and Dubois [17, 3], the TO and RD tilings are both more "efficient" spatial samplers than the cubic grid. That is, for a 3-D band-limited signal which is spherically symmetric in the frequency domain, we require fewer samples on a TO or RD grid to fully reconstruct the signal (that is, to meet the Nyquist sampling criterion for all spatial frequencies) than we do on a cubic grid. The number of samples needed is proportional to the volume of the minimum grid shape which can bound the unit sphere. For example, this is equal to 8.0 for a cubic tiling but only $4\sqrt{2} \approx 5.657$ for the RD tiling. Hence, one can sample space about 41 percent more efficiently with an RD grid.

4.3.2. Topology: Thinning Algorithms and Finite Element Methods

Working with TO grids might also simplify 3-D thinning algorithms, since like hexagons in 2-D, there is no neighborhood ambiguity on a TO grid [8]. This could greatly simplify analyses such as those found in [19, 11, 15]. Such neighborhood consistency properties are also desirable in certain finite element modeling applications.

4.3.3. Geometry of Construction

Finally, we consider a few implications of tiling choices in applications where solid voxels are used to conform as closely as possible to a given shape. For example, in creating a foundation using "bricks" of a fixed shape along a boundary whose shape is unknown in advance, the TO grid gives us a smaller surface area boundary than the cubic tiling. As seen from Table 2, the TO grid is the winner in this category with a mean area of 1.455 units compared with 1.5 units for that of the cube and the RD. Minimizing exposure to the elements in a construction project by minimizing surface area using this method represents a potential application.

4.4. Future Work

While we have shown that the rhombic dodecahedron outperforms the truncated octahedron and the cube for the computation of surface area, we have not shown that this is the optimal solid for the job. If we restrict our choices to space-filling parallelohedra (volumes which can fill space through simple parallel displacement), then we must also analyze the triangular prism, the hexagonal prism, and another 14-hedron which tiles space.

As already suggested, random and pseudo-random tilings represent possible interesting solutions to boundary estimate problems, depending on the nature of the problem [9]. Further investigation into these is certainly warranted.

Though this paper focussed on local counting algorithms, there is also potential for the aforementioned tessellations in improving non-local schemes for computing area. Such algorithms may become significantly more efficient or simple when employing these grids rather than the conventional rectangular prism grids.

Appendix A. Some Identities

The following identities were derived using several equivalences we came across during our analyses. They were used heavily in the derivation of closed form expressions for the area biases for truncated octahedral and rhombic dodecahedral tilings. They are based on two

sets of observations, the first having to do with symmetries of certain functions on the unit sphere and the second stemming from different parameterizations of families of planes. Many more such identities could be derived, but these give the basic flavor of the ones which were used in deriving the results in this paper. The main use of these identities was to make difficult integrals easier to solve. In particular, many of the integrals involving the arctan function were simplified in this manner.

1.1. Regions of Symmetry

Recall that the estimated area function for the cube is given by

$$A_C(\theta, \phi) = \sin\phi + \cos\phi\cos\theta + \cos\phi\sin\theta \tag{37}$$

Then, by symmetry of coordinates we have the following:

$$\int_0^{\frac{\pi}{4}} \int_0^{\arctan(\cos\theta)} A_C(\theta, \phi)\cos\phi \, d\phi \, d\theta \tag{38}$$

$$= \int_{\frac{\pi}{4}}^{\frac{\pi}{2}} \int_0^{\arctan\left(\cos\left(\frac{\pi}{2}-\theta\right)\right)} A_C(\theta, \phi)\cos\phi \, d\phi \, d\theta \tag{39}$$

$$= 2 \times \int_0^{\frac{\pi}{4}} \int_{\arctan(\cos\theta)}^{\frac{\pi}{2}} A_C(\theta, \phi)\cos\phi \, d\phi \, d\theta \tag{40}$$

$$= 2 \times \int_{\frac{\pi}{4}}^{\frac{\pi}{2}} \int_{\arctan(\cos\theta)}^{\frac{\pi}{2}} A_C(\theta, \phi)\cos\phi \, d\phi \, d\theta \tag{41}$$

1.2. Alternative Parameterizations of Planar Segments

A family of planes represented by a lune on the unit sphere (as in Figure 9) is described by the range of two parameters, ϕ and θ. Different geometrical interpretations of these parameters (but which represent the same family of planes) give rise to different formulas for computing statistics of these families of planes.

For example, in the case of computing the area bias for cubes, it is useful to consider

these parameters to represent the angular deviation of a plane's normal from the z-axis. However, in the case of the rhombic dodecahedron, it is more convenient to consider these angles to be the angles formed between the plane and the x- and y-axes respectively.

These different interpretations lead to multiple expressions for the same quantity, which are expressed in the following identities:

$$\int_0^{\frac{\pi}{4}} \int_0^{\arctan(\cos\theta)} (\cos\phi\cos\theta)\cos\phi\, d\phi\, d\theta \tag{42}$$

$$= \int_{\frac{\pi}{4}}^{\frac{\pi}{2}} \int_0^{\arctan\left(\cos\left(\frac{\pi}{2}-\theta\right)\right)} (\cos\phi\sin\theta)\cos\phi\, d\phi\, d\theta \tag{43}$$

$$= 2\times\int_0^{\frac{\pi}{4}} \int_{\arctan(\cos\theta)}^{\frac{\pi}{2}} (\sin\phi)\cos\phi\, d\phi\, d\theta \tag{44}$$

$$= 2\times\int_{\frac{\pi}{4}}^{\frac{\pi}{2}} \int_{\arctan\left(\cos\left(\frac{\pi}{2}-\theta\right)\right)}^{\frac{\pi}{2}} (\sin\phi)\cos\phi\, d\phi\, d\theta. \tag{45}$$

Similarly, we have:

$$\int_0^{\frac{\pi}{4}} \int_0^{\arctan(\cos\theta)} (\sin\phi)\cos\phi\, d\phi\, d\theta \tag{46}$$

$$= \int_{\frac{\pi}{4}}^{\frac{\pi}{2}} \int_0^{\arctan\left(\cos\left(\frac{\pi}{2}-\theta\right)\right)} (\sin\phi)\cos\phi\, d\phi\, d\theta \tag{47}$$

$$= \int_{\frac{\pi}{4}}^{\frac{\pi}{2}} \int_0^{\arctan\left(\cos\left(\frac{\pi}{2}-\theta\right)\right)} (\cos\phi\cos\theta)\cos\phi\, d\phi\, d\theta \tag{48}$$

$$= \int_0^{\frac{\pi}{4}} \int_{\arctan(\cos\theta)}^{\frac{\pi}{2}} (\cos\phi\cos\theta)\cos\phi\, d\phi\, d\theta + \int_{\frac{\pi}{4}}^{\frac{\pi}{2}} \int_{\arctan\left(\cos\left(\frac{\pi}{2}-\theta\right)\right)}^{\frac{\pi}{2}} (\cos\phi\cos\theta)\cos\phi\, d\phi\, d\theta \tag{49}$$

$$= \int_0^{\frac{\pi}{4}} \int_{\arctan(\cos\theta)}^{\frac{\pi}{2}} (\cos\phi \sin\theta) \cos\phi \, d\phi \, d\theta$$

$$+ \int_{\frac{\pi}{4}}^{\frac{\pi}{2}} \int_{\arctan\left(\cos\left(\frac{\pi}{2}-\theta\right)\right)}^{\frac{\pi}{2}} (\cos\phi \sin\theta) \cos\phi \, d\phi \, d\theta \tag{50}$$

$$= \int_0^{\frac{\pi}{4}} \int_0^{\arctan(\cos\theta)} (\cos\phi \sin\theta) \cos\phi \, d\phi \, d\theta. \tag{51}$$

Appendix B. Derivation of Closed Form Solutions to Mean Estimated Area Integrals

2.1. The Truncated Octahedron Grid

Here we present the derivation of the mean surface area estimates for the truncated octahedron grid. To remind the reader, from Eq. (33), we have

$$A_T(\phi, \theta) = \left(\frac{1}{4} + \frac{3}{4}\sqrt{3}\right) \sin\phi + \frac{1}{4} \sin\theta \cos\phi + \frac{1}{4} \cos\phi \cos\theta, \quad \{\forall (\phi, \theta) \in C\}, \tag{52}$$

as the estimated area formula as a function of the planar segment normals, for planar segments whose normals fall within Region C of Figure 9. The integral for mean estimated area is then that shown on the left hand side of Eq. (34). We compute its value below:

$$\frac{\int\int_C A_T(\phi,\theta) \cos\phi \, d\phi \, d\theta}{\int\int_C \cos\phi \, d\phi \, d\theta} \tag{53}$$

$$= \frac{\int\int_C \left(\left(\frac{1}{4}+\frac{3}{4}\sqrt{3}\right) \sin\phi + \frac{1}{4} \sin\theta \cos\phi + \frac{1}{4} \cos\phi \cos\theta\right) \cos\phi \, d\phi \, d\theta}{\frac{\pi}{6}} \tag{54}$$

$$= \frac{\int\int_C \left(\frac{1}{4} \sin\phi + \frac{1}{4} \sin\theta \cos\phi + \frac{1}{4} \cos\phi \cos\theta\right) \cos\phi \, d\phi \, d\theta + \int\int_C \left(\frac{3}{4}\sqrt{3} \sin\phi\right) \cos\phi \, d\phi \, d\theta}{\frac{\pi}{6}} \tag{55}$$

$$= \frac{\int\int_C \frac{1}{4}(\sin\phi + \sin\theta \cos\phi + \cos\phi \cos\theta) \cos\phi \, d\phi \, d\theta + \int\int_C \left(\frac{3}{4}\sqrt{3} \sin\phi\right) \cos\phi \, d\phi \, d\theta}{\frac{\pi}{6}} \tag{56}$$

$$= \frac{\frac{1}{4}\frac{\pi}{4} + \frac{3\sqrt{3}}{4}\left(\int_0^{\frac{\pi}{4}}\int_{\arctan(\cos\theta)}^{\frac{\pi}{2}} (\sin\phi)\cos\phi\, d\phi\, d\theta + \int_{\frac{\pi}{4}}^{\frac{\pi}{2}}\int_{\arctan\left(\cos\left(\frac{\pi}{2}-\theta\right)\right)}^{\frac{\pi}{2}} (\sin\phi)\cos\phi\, d\phi\, d\theta\right)}{\frac{\pi}{6}} \tag{57}$$

$$= \frac{\frac{\pi}{16} + \frac{3\sqrt{3}}{4}\left(2 \times \int_0^{\frac{\pi}{4}}\int_{\arctan(\cos\theta)}^{\frac{\pi}{2}} (\sin\phi)\cos\phi\, d\phi\, d\theta\right)}{\frac{\pi}{6}} \tag{58}$$

$$= \frac{\frac{\pi}{16} + \frac{3\sqrt{3}}{4}\left(\int_0^{\frac{\pi}{4}} \left(\sin^2\phi|_{\arctan(\cos\theta)}^{\frac{\pi}{2}}\right) d\theta\right)}{\frac{\pi}{6}} \tag{59}$$

$$= \frac{\frac{\pi}{16} + \frac{3\sqrt{3}}{4}\left(\int_0^{\frac{\pi}{4}} \left(1 - \frac{\cos^2\theta}{1+\cos^2\theta}\right)\right) d\theta}{\frac{\pi}{6}} \tag{60}$$

$$= \frac{\frac{\pi}{16} + \frac{3\sqrt{3}}{4}\left(\int_0^{\frac{\pi}{4}} \frac{1}{1+\cos^2\theta}\right) d\theta}{\frac{\pi}{6}} \tag{61}$$

$$= \frac{\frac{\pi}{16} + \frac{3\sqrt{3}}{4}\left(\frac{\arctan\left(\frac{\tan\theta}{\sqrt{2}}\right)}{\sqrt{2}}|_0^{\frac{\pi}{4}}\right)}{\frac{\pi}{6}} \tag{62}$$

$$= \frac{\frac{\pi}{16} + \frac{3\sqrt{6}}{8} \times \arctan\frac{1}{\sqrt{2}}}{\frac{\pi}{6}}. \tag{63}$$

Explanations of some of the steps follow. Eq.(55) separates the integral into two parts, one of which is 1/4 of the cubic grid integral we previously computed. This allows us in Eq.(57) to reduce the left term in the numerator to 1/4 times $\pi/4$. In Eq.(58), we have used the symmetry of the two halves of Region C in Figure 9. This could also be inferred from the identities of Eq.(40) and Eq.(41). The rest of the analysis is straight forward calculus.

2.2. The Rhombic Dodecahedron Grid

Here we present the derivation of the mean surface area estimates for the rhombic dodecahedron grid. Before proceeding with the body of the derivation, it will be useful to have the

following lemma:

$$\int_0^{\frac{\pi}{4}} \left(\arctan\left(\cos\theta\right) + \frac{\cos\theta}{1+\cos^2\theta} \right) \cos\theta \, d\theta = 2\frac{\arctan\frac{1}{\sqrt{2}}}{\sqrt{2}}. \tag{64}$$

To prove this we note that

$$\begin{aligned}
& 2\int_0^{\frac{\pi}{4}} \int_0^{\arctan(\cos\theta)} (\cos\phi\cos\theta)\cos\phi \, d\phi \, d\theta && (65)\\
= \; & 2\int_0^{\frac{\pi}{4}} \int_0^{\arctan(\cos\theta)} \cos^2\phi\cos\theta \, d\phi \, d\theta && (66)\\
= \; & 2\int_0^{\frac{\pi}{4}} \int_0^{\arctan(\cos\theta)} \left(\frac{1+\cos 2\phi}{2}\right)\cos\theta \, d\phi \, d\theta && (67)\\
= \; & \int_0^{\frac{\pi}{4}} \left(\phi + \frac{\sin 2\phi}{2}\right)\cos\theta\Big|_0^{\arctan(\cos\theta)} d\theta && (68)\\
= \; & \int_0^{\frac{\pi}{4}} \left(\phi + \sin\phi\cos\phi\right)\cos\theta\Big|_0^{\arctan(\cos\theta)} d\theta && (69)\\
= \; & \int_0^{\frac{\pi}{4}} \left(\arctan\left(\cos\theta\right) + \frac{\cos\theta}{1+\cos^2\theta} \right) \cos\theta \, d\theta, && (70)
\end{aligned}$$

which is the left hand side of the lemma, and starting from the same expression we can also produce

$$\begin{aligned}
& 2\int_0^{\frac{\pi}{4}} \int_0^{\arctan(\cos\theta)} (\cos\phi\cos\theta)\cos\phi \, d\phi \, d\theta && (71)\\
= \; & 2\left(2\int_0^{\frac{\pi}{4}} \int_{\arctan(\cos\theta)}^{\frac{\pi}{2}} (\sin\phi)\cos\phi \, d\phi \, d\theta\right) && (72)\\
= \; & 2\frac{\arctan\frac{1}{\sqrt{2}}}{\sqrt{2}}, && (73)
\end{aligned}$$

which is the right hand side of the lemma expression. The step of Eq.(72) uses the identities of Eq.(42) and Eq.(44). The step of Eq.(73) duplicates part of the derivation in the immediately

preceding derivation for the truncated octahedron, namely, the steps of Eq.(58) through Eq.(63). This completes the proof of the lemma.

From Eq. (36), we have

$$A_R(\phi,\theta) = \sqrt{2}\sin\phi + \frac{1}{2}\cos\phi\cos\left(\theta+\frac{\pi}{4}\right) + \frac{1}{2}\cos\phi\sin\left(\theta+\frac{\pi}{4}\right), \quad \{\forall\,(\phi,\theta)\in C_L\}, \quad (74)$$

as the estimated area formula as a function of the planar segment normals, for planar segments whose normals fall within the left half of Region C of Figure 9. The mean estimated area is then

$$\frac{\int\int_{C_L} A_R(\phi,\theta)\cos\phi\,d\phi\,d\theta}{\int\int_{C_L}\cos\phi\,d\phi\,d\theta} \quad (75)$$

$$= \frac{\int\int_{C_L}\left(\sqrt{2}\sin\phi+\frac{1}{2}\cos\phi\cos\left(\theta+\frac{\pi}{4}\right)+\frac{1}{2}\cos\phi\sin\left(\theta+\frac{\pi}{4}\right)\right)\cos\phi\,d\phi\,d\theta}{\frac{\pi}{12}} \quad (76)$$

$$= \frac{\int\int_{C_L}\left(\sqrt{2}\sin\phi+\frac{\sqrt{2}}{2}\cos\phi\cos\theta\right)\cos\phi\,d\phi\,d\theta}{\frac{\pi}{12}} \quad (77)$$

$$= \frac{\sqrt{2}\int\int_{C_L}(\sin\phi)\cos\phi\,d\phi\,d\theta + \int\int_{C_L}\frac{\sqrt{2}}{2}\cos^2\phi\cos\theta\,d\phi\,d\theta}{\frac{\pi}{12}} \quad (78)$$

$$= \frac{\sqrt{2}\int\int_{C_L}(\sin\phi)\cos\phi\,d\phi\,d\theta + \frac{\sqrt{2}}{4}\int\int_{C_L}(1+\cos 2\phi)\cos\theta\,d\phi\,d\theta}{\frac{\pi}{12}} \quad (79)$$

$$= \frac{\sqrt{2}\frac{\arctan\left(\frac{1}{\sqrt{2}}\right)}{2\sqrt{2}} + \frac{\sqrt{2}}{4}\int_0^{\frac{\pi}{4}}\left(\phi+\frac{\sin 2\phi}{2}\right)|_{\arctan(\cos\theta)}^{\frac{\pi}{2}}\cos\theta\,d\theta}{\frac{\pi}{12}} \quad (80)$$

$$= \frac{\frac{\arctan\left(\frac{1}{\sqrt{2}}\right)}{2} + \frac{\sqrt{2}}{4}\int_0^{\frac{\pi}{4}}\left(\frac{\pi}{2}-\left(\arctan(\cos\theta)+\frac{\sin(2\arctan(\cos\theta))}{2}\right)\right)\cos\theta\,d\theta}{\frac{\pi}{12}} \quad (81)$$

$$= \frac{\frac{\arctan\left(\frac{1}{\sqrt{2}}\right)}{2}}{\frac{\pi}{12}} + \frac{\frac{\sqrt{2}}{4}\int_0^{\frac{\pi}{4}}\left(\frac{\pi}{2}-(\arctan(\cos\theta)+\sin(\arctan(\cos\theta))\cos(\arctan(\cos\theta)))\right)\cos\theta d\theta}{\frac{\pi}{12}} \quad (82)$$

$$= \frac{\frac{\arctan\left(\frac{1}{\sqrt{2}}\right)}{2} + \frac{\sqrt{2}}{4}\int_0^{\frac{\pi}{4}} \left(\frac{\pi}{2} - \left(\arctan\left(\cos\theta\right) + \frac{\cos\theta}{1+\cos^2\theta}\right)\right)\cos\theta\, d\theta}{\frac{\pi}{12}} \tag{83}$$

$$= \frac{\frac{\arctan\left(\frac{1}{\sqrt{2}}\right)}{2} + \frac{\sqrt{2}}{4}\left(\int_0^{\frac{\pi}{4}} \frac{\pi}{2}\cos\theta\, d\theta - \int_0^{\frac{\pi}{4}} \left(\arctan\left(\cos\theta\right) + \frac{\cos\theta}{1+\cos^2\theta}\right)\cos\theta\, d\theta\right)}{\frac{\pi}{12}} \tag{84}$$

$$= \frac{\frac{\arctan\left(\frac{1}{\sqrt{2}}\right)}{2} + \frac{\sqrt{2}}{4}\left(\int_0^{\frac{\pi}{4}} \frac{\pi}{2}\cos\theta\, d\theta - 2\frac{\arctan\frac{1}{\sqrt{2}}}{\sqrt{2}}\right)}{\frac{\pi}{12}} \tag{85}$$

$$= \frac{\frac{\arctan\left(\frac{1}{\sqrt{2}}\right)}{2} + \frac{\sqrt{2}}{4}\left(\frac{\pi}{2}\frac{\sqrt{2}}{2} - 2\frac{\arctan\frac{1}{\sqrt{2}}}{\sqrt{2}}\right)}{\frac{\pi}{12}} \tag{86}$$

$$= \frac{\frac{\arctan\left(\frac{1}{\sqrt{2}}\right)}{2} + \frac{\pi}{8} - \frac{\arctan\left(\frac{1}{\sqrt{2}}\right)}{2}}{\frac{\pi}{12}} \tag{87}$$

$$= \frac{3}{2}. \tag{88}$$

Well that was a lot of work to get an answer of 3/2! Explanations of some of the steps follow. Eq.(76) uses the standard sum of angles identity. Eq.(79) uses the results from the TO derivation to produce the arctan expression of the leftmost term in Eq.(70). Eq.(81) applies the double angle identity for sin. Finally, Eq.(84) uses the lemma proved above to simplify the nasty integral.

Acknowledgements

I thank the reviewers for their comments; they greatly improved this work. I thank Professor Berthold K. P. Horn and Chris Stauffer for valuable feedback regarding this work. This work was supported by the Office of Naval Research, Grant No. N00014-96-1-0311.

Bibliography

[1] Nadim M. Aziz and Sudarshan P. Bhat. On the computation of integral properties of objects. *Advances in Engineering Software*, 12(4):174–180, 1990.

[2] E. S. Deutsch. Thinning algorithms on rectangular, hexagonal, and triangular arrays. *Communications of the ACM*, 15:827–837, 1972.

[3] Eric Dubois. The sampling and reconstruction of time-varying imagery with application in video systems. *Proceedings of the IEEE*, 73(4):502–522, 1985.

[4] Peter C. Gasson. *Geometry of Spatial Forms: Analysis, Synthesis, Concept Formulation and Space Vision for CAD.* Ellis Horwood Limited, Chicester, England, 1983.

[5] M. J. E. Golay. Hexagonal parallel pattern transformations. *IEEE Transactions on Computers*, pages 733–740, 1969.

[6] S. B. Gray. Local properties of binary images in two dimensions. *IEEE Transactions on Computers*, pages 551–561, 1971.

[7] Innchyn Her and Chi-Tseng Yuan. Resampling on a pseudohexagonal grid. *CVGIP: Graphical Models and Image Processing*, 56(4):336–347, 1994.

[8] Berthold K. P. Horn. *Robot Vision.* MIT Press, Cambridge, Massachusetts, 1986.

[9] Sanjeev R. Kulkarni, Sanjoy K. Mitter, T. J. Richardson, and John N. Tsitsiklis. Local versus nonlocal computation of length in digitized curves. *IEEE Transactions on Pattern Analysis and Machine Intelligence*, 16:711–718, 1994.

[10] L. J. Latecki, C. Conrad, and A. Gross. Preserving topology by a digitization process. *Journal of Mathematical Imaging and Vision*, 8:131–159, 1998.

[11] Chung-Nim Lee, Timothy Poston, and Azriel Rosenfeld. Winding and Euler numbers for 2D and 3D digital images. *CVGIP: Image Understanding*, 53(6):522–537, 1991.

[12] Yong Tsui Lee and Aristides A. G. Requicha. Algorithms for computing the volume and other integral properties of solids. I. Known methods and open issues. *Communications of the ACM*, 25(9):635–641, 1982.

[13] Yong Tsui Lee and Aristides A. G. Requicha. Algorithms for computing the volume and other integral properties of solids. II. A family of algorithms based on representation conversion and cellular approximation. *Communications of the ACM*, 25(9):642–650, 1982.

[14] L. A. Lyusternik. *Convex Figures and Polyhedra*. Dover, New York, New York, 1963.

[15] Cheng Min Ma. On topology preservation in 3D thinning. *CVGIP: Image Understanding*, 59(3):328–339, 1994.

[16] Greg McCarthy and Marie Luby. Imaging the structural changes associated with human epilepsy. *Clinical Neuroscience*, 2:82–88, 1994.

[17] Russell M. Mersereau. The processing of hexagonally sampled two-dimensional signals. *Proceedings of the IEEE*, 67(6):930–949, 1979.

[18] R. G. Petty, G. Pearlson, I. McGilchrist, R. Lewis, A. Y. Tien, A. Pulver, D. D. Vaughn, M. F. Casanova, R. E. Powers, and P. E. Barta. Reversal of asymmetry of the planum temporale in schizophrenia. *American Journal of Psychiatry*, 152:715–721, 1995.

[19] P. K. Saha and B. B. Chaudhuri. 3D digital topology under binary transformation with applications. *Computer Vision and Image Understanding*, 63:418–429, 1996.

[20] Luis A. Santalo. *Integral Geometry and Geometric Proabability*. Addison-Wesley, Reading, Massachusetts, 1976.

[21] Eric W. Weisstein. Eric's treasure trove of mathematics. *World Wide Web Document: http://astsun.astro.virginia.edu/~ eww6n/math/*, 1997.

[22] Stephen Wolfram. *The Mathematica Book, 3rd Edition.* Wolfram Media, Champaign, Illinois, 1996.